Journal of Computational Physics 430 (2021) 110090

Contents lists available at ScienceDirect

Journal of Computational Physics

www.elsevier.com/locate/jcp

An immersed boundary projection method for incompressible interface simulations in 3D flows

Kian Chuan Ong [a], Ming-Chih Lai [b], Yunchang Seol [b,*]

[a] Fields Institute for Research in Mathematical Sciences, 222 College Street, Toronto, Ontario, M5T3J1 Canada
[b] Department of Applied Mathematics, National Chiao Tung University, 1001 Ta Hsueh Road, Hsinchu 300, Taiwan

ARTICLE INFO

Article history:
Available online 30 December 2020

Keywords:
Immersed boundary projection method
Fractional step method
Incompressible interface
Triangulated surface

ABSTRACT

In this paper, we extend our previous immersed boundary (IB) projection method for 2D inextensible vesicle in unsteady Stokes flow (Ong and Lai, 2020 [23]) to 3D incompressible interface as a prototype of vesicles. In spite of similar numerical algorithm to the 2D case, the present 3D numerical implementation is far from straightforward. An incompressible interface immersed in Newtonian fluid must ensure both conservative constraints associated with local fluid volume and local interfacial area. To accomplish this, we triangulate the incompressible interface, whereby the unknown elastic tension is defined on the triangles, while the associated tension force term is defined at vertices (Lagrangian markers). Consistent approximations of surface differential operators on a triangulated interface are developed accordingly. An extra scalar field is introduced in the IB projection approach so that the fluid pressure and interfacial elastic tension are efficiently solved in a divide-and-conquer manner. As a result, the local interfacial and volumetric incompressibilities can be ideally satisfied simultaneously. A series of numerical tests on the present scheme is performed to verify the robustness and applicability of the method. We first carry out the convergence study of the solution variables defined on the fluid and interface. We then study the shear-induced deformations of incompressible interface for various initial configurations. At last, the bending force and the penalty force for improved volume conservation are further incorporated into our method to simulate an oblate vesicle dynamics in quiescent flow.

1. Introduction

Lipid-bilayer vesicle has been extensively studied due to not only its importance but also the similarity of biological behaviors with red blood cells [29,22]. It is well-known that interfacial forces of vesicle model consist of interfacial incompressibility and bending resistance [1,9]. The purely incompressible interface without bending force can also be regarded as a prototype of the vesicle. For this reason, in this paper, we focus on the study of incompressible interfacial motion in unsteady Stokes flow. Mathematically, the interfacial incompressibility is equivalent to the surface divergence-free condition, as shown in [30,28]. This condition is analogous to the volumetric divergence-free condition associated with an incompressible fluid. For instance, the fluid pressure in Navier-Stokes equations enforces the volumetric divergence-free condition to conserve the local fluid volume. Likewise, the interfacial elastic tension imposes the surface divergence-free condition

* Corresponding author.
E-mail addresses: kong@fields.utoronto.ca (K.C. Ong), mclai@math.nctu.edu.tw (M.-C. Lai), ycseol@math.nctu.edu.tw (Y. Seol).

https://doi.org/10.1016/j.jcp.2020.110090
0021-9991/

of interfacial velocity to conserve the local surface area. Hence, the pressure and the elastic tension both act as Lagrange multipliers for the fluid incompressibility and the interface incompressibility, respectively.

In 3D Stokes flow, the boundary integral method is popular due to its computational efficiency and accuracy [39,17,5, 33,38]. For an incompressible interface $\mathbf{X}$, it allows to represent the solution of boundary velocity by $\mathbf{u}(\mathbf{X}) = \mathbf{G}(\sigma)$, where the unknown elastic tension σ defined on the interface shall be solved to enforce the interfacial incompressibility $\nabla_s \cdot \mathbf{u} = 0$ and the function $\mathbf{G}$ is a boundary integral expressed by Green's function automatically satisfying the volumetric incompressibility of fluid $\nabla \cdot \mathbf{u} = 0$. To find σ, we apply the surface divergence operator $\nabla_s \cdot$ on both sides, then solve $\nabla_s \cdot \mathbf{G}(\sigma) = 0$. Thus, the interfacial incompressibility can be readily satisfied by using the elastic tension without violating the volumetric incompressibility constraint.

Apart from the boundary integral method, the development of a grid-based numerical method simultaneously satisfying the above two conditions is still a major difficulty of modeling the fluidic incompressible interface in Stokes flow. In discretization using a uniform grid in fluid domain and a triangulation on the interface, the fluid velocity is coupled with the fluid pressure p and the elastic tension σ via the fluid and interface incompressibility conditions so a linear system involving all solution variables must be solved. In this paper, instead of solving a whole linear system, we extend our previous immersed boundary (IB) projection method for two dimensional inextensible interface [23] to three dimensions. Our main advantage is to solve all solution variables in a divide-and-conquer manner so that each solution variable can be solved individually as you can see the summary of our algorithm later. In addition, the fluid velocity and pressure can be solved very efficiently via FFT-based elliptic solvers. However, like the boundary integral method mentioned before, the tension here is solved via GMRES iterative method which might cause an increase in the number of iterations as the fluid and interfacial grids refine. Since the interface is moving, finding an effective preconditioner of GMRES iteration poses another challenge in present scheme as well as the boundary integral method. Fortunately, the elastic tension is one dimension lower degree of freedom than the fluid variables so the computational cost is acceptable.

To overcome the above mentioned difficulties, a four-step projection method based on level-set was developed in [26], and later an iterative technique was used in [27]. It was further improved in [16] to enforce two constraints simultaneously by partitioning the whole system via Schur complement as in [18]. The level-set formulation employs an implicit representation of interface as the zero contour. As the implicit interface evolves, the constraint of local interfacial incompressibility is hard to maintain in time. So in [16], an extra global constraint is enforced to conserve the total interfacial area on top of the local constraint. The phase-field or diffuse interface method also represents the interface implicitly. To enforce the local condition in [2], the interfacial stretching factor is tracked according to an advection and diffusion equation. Similarly, in [4], the elastic tension field defined on a bulk fluid is evolved to achieve the same purpose. As indicated, for such interface capturing methods, a special algorithm must be designed carefully to preserve the local interfacial incompressibility.

In this paper, we employ the immersed boundary (IB) method [24,25] which represents the interface explicitly. Unlike the interface capturing methods described above, the IB method enables us to track all the geometric elements of the immersed interface; thus, enforcing local interfacial incompressibility is more straightforward. Our concern here is to simultaneously satisfy both local constraints with respect to interfacial area and fluid volume. In 1977 [24], Peskin presented a spring-like penalty force to model the inextensible heart valve leaflets. Later by Lai et al., a generalization of the penalty approach for local interfacial incompressibility was proposed to model 3D axisymmetric vesicle [12] and fully 3D triangulated vesicle [28]. One may refer to a similar approach in [36]. To find the elastic tension rather than the artificial one using penalty parameter, the penalty IB method in [14] is employed to model vesicles by virtually decoupling both the vesicle configuration and the nearby fluid flow. Nevertheless, the method still suffers from the usage of large penalty parameter (thus small time step) to link those dual interfaces. Recently, the first two authors of this paper have developed an IB projection method [31] for simulating 2D vesicle dynamics without any penalization [23]. By using block LU decomposition of the resultant linear system, all solution variables including the fluid velocity, fluid pressure, and the elastic tension can be solved individually and efficiently. More importantly, the proposed method satisfies the interfacial and volumetric incompressibilities in discrete sense simultaneously.

The main contributions of this paper are twofold. Firstly, we extend the IB projection method in [23] to simulate the motion of a fully 3D triangulated incompressible interface, so both local constraints are satisfied without using penalty parameters. For doing this, appropriate approximations of discrete differential operators must be chosen; in particular, a simple formula for computing elastic tension force is derived from the discrete tension energy on a triangular mesh. Secondly, an algorithm for long-time simulations is developed to conserve better the local interfacial area. The idea is to modify the discrete surface divergence of interfacial velocity by imposing a correction term that is derived from the transport equation of the local interfacial area. By virtue of the IB method, the conservation of the total interfacial area is naturally followed by enforcing the local constraint.

The rest of this paper is organized as follows. Firstly, we present the governing equations based on the immersed boundary framework, which describes an incompressible interface dynamics in unsteady Stokes flow. In Section 3, the IB projection method for a triangulated incompressible interface is presented in conjunction with the proper approximations of discrete surface differential operators. Next, an improved conservation method of the local interfacial area is proposed and discussed. In Section 4, a series of the numerical experiments is performed to study the convergence behaviors of the present method and the effects of different initial configurations on the interfacial motion under shear flow. To show the applicability of our method, we further consider the extra interfacial forces such as bending force and penalty force for improved volume conservation. Conclusion and future work are given in Section 5.

2. Governing equations of motion

In the present study, we are interested in modeling and simulating the incompressible interface immersed in unsteady Stokes flow. Once this model is developed, the extra interfacial force such as the bending force can be coupled easily into the model (see the numerical test in Subsection 4.4), so this is regarded as a prototype of the vesicle or red blood cell problems. Consider the governing equations for an incompressible closed interface immersed in a three-dimensional incompressible viscous fluid domain Ω as

$$\frac{\partial \mathbf{u}}{\partial t} + \nabla p = \mu \Delta \mathbf{u} + S[\sigma] \quad \text{in } \Omega, \tag{1}$$

$$\nabla \cdot \mathbf{u} = 0 \quad \text{in } \Omega, \tag{2}$$

$$S[\sigma] = \int_\Gamma \mathbf{F}_\sigma \, \delta(\mathbf{x} - \mathbf{X}(\alpha, \beta, t)) \, \mathrm{d}A = \int_\Gamma (\nabla_s \sigma - 2\sigma H \mathbf{n}) \, \delta(\mathbf{x} - \mathbf{X}(\alpha, \beta, t)) \, \mathrm{d}A, \tag{3}$$

$$\frac{\partial \mathbf{X}}{\partial t}(\alpha, \beta, t) = \mathbf{U}(\alpha, \beta, t) := \widehat{S}[\mathbf{u}] = \int_\Omega \mathbf{u}(\mathbf{x}, t) \, \delta(\mathbf{x} - \mathbf{X}(\alpha, \beta, t)) \, \mathrm{d}\mathbf{x} \quad \text{on } \Gamma, \tag{4}$$

$$\nabla_s \cdot \mathbf{U} = 0 \quad \text{on } \Gamma, \tag{5}$$

where $\mathbf{u}(\mathbf{x}, t)$ is the fluid velocity, $p(\mathbf{x}, t)$ is the fluid pressure, μ is the kinematic viscosity, and $\mathbf{x} = (x, y, z)$ is the Cartesian coordinates in Ω. The closed interface Γ as an immersed boundary is represented by a set of Lagrangian markers $\mathbf{X}(\alpha, \beta, t)$ with two parameters α and β. The notations such as H and $\mathbf{n}$ represent the mean curvature and the outward unit normal vector of Γ, respectively. The elastic tension force of Γ is defined by $\mathbf{F}_\sigma = \nabla_s \sigma - 2\sigma H \mathbf{n}$ in Eq. (3), where the elastic tension σ acts as an unknown Lagrange multiplier to enforce the surface incompressibility (5). To close the system (1)-(5), the initial and boundary conditions for the fluid velocity and the initial interface configuration must be given.

To proceed, we shall introduce some preliminary surface differential geometry [7] to express the mathematical forms for the surface gradient ∇_s and surface divergence $\nabla_s \cdot$ used in above formulation. For a surface patch $\mathbf{X}(\alpha, \beta)$ at fixed time, the coefficients of the first fundamental form are defined by

$$E = \mathbf{X}_\alpha \cdot \mathbf{X}_\alpha, \quad F = \mathbf{X}_\alpha \cdot \mathbf{X}_\beta, \quad G = \mathbf{X}_\beta \cdot \mathbf{X}_\beta,$$

where the subscripts α and β of a function denote its partial derivatives of the function with respect to α and β, respectively. So the local area stretching factor can be written as $\|\mathbf{X}_\alpha \times \mathbf{X}_\beta\|_2 = \sqrt{EG - F^2}$. The local surface area in Eq. (3) can be defined by $\mathrm{d}A = \|\mathbf{X}_\alpha \times \mathbf{X}_\beta\|_2 \mathrm{d}\alpha \mathrm{d}\beta = \sqrt{EG - F^2} \mathrm{d}\alpha \mathrm{d}\beta$. We define the unit normal vector as $\mathbf{n} = \mathbf{X}_\alpha \times \mathbf{X}_\beta / \|\mathbf{X}_\alpha \times \mathbf{X}_\beta\|_2$, where $\|\cdot\|_2$ stands for the Euclidean norm. The coefficients of the second fundamental form are defined by

$$L = \mathbf{X}_{\alpha\alpha} \cdot \mathbf{n} = -\mathbf{X}_\alpha \cdot \mathbf{n}_\alpha, \quad M = \mathbf{X}_{\alpha\beta} \cdot \mathbf{n} = -\mathbf{X}_\alpha \cdot \mathbf{n}_\beta = -\mathbf{X}_\beta \cdot \mathbf{n}_\alpha, \quad N = \mathbf{X}_{\beta\beta} \cdot \mathbf{n} = -\mathbf{X}_\beta \cdot \mathbf{n}_\beta,$$

and the mean curvature of the surface can be obtained from $H = \frac{-GL - EN + 2FM}{2(EG - F^2)}$.

Using the fundamental forms, the surface gradient $\nabla_s \sigma$ of a scalar function σ can be represented by

$$\nabla_s \sigma = \frac{G\sigma_\alpha - F\sigma_\beta}{EG - F^2} \mathbf{X}_\alpha + \frac{E\sigma_\beta - F\sigma_\alpha}{EG - F^2} \mathbf{X}_\beta. \tag{6}$$

In a similar fashion, the surface divergence $\nabla_s \cdot \mathbf{U}$ of a vector field $\mathbf{U}$ can be represented by

$$\nabla_s \cdot \mathbf{U} = \frac{G\mathbf{U}_\alpha - F\mathbf{U}_\beta}{EG - F^2} \cdot \mathbf{X}_\alpha + \frac{E\mathbf{U}_\beta - F\mathbf{U}_\alpha}{EG - F^2} \cdot \mathbf{X}_\beta. \tag{7}$$

Meanwhile, as introduced in [19], Eq. (7) can be alternatively expressed by

$$\nabla_s \cdot \mathbf{U} = \frac{(\mathbf{X}_\beta \times \mathbf{n}) \cdot \mathbf{U}_\alpha + (\mathbf{n} \times \mathbf{X}_\alpha) \cdot \mathbf{U}_\beta}{\|\mathbf{X}_\alpha \times \mathbf{X}_\beta\|_2}, \tag{8}$$

so in the next section, we will use this to define the discrete surface divergence operator on a triangulated surface. The elastic tension force consists of the tangential component $\nabla_s \sigma$ and the normal component $\sigma H \mathbf{n}$. In our prior study [28], each component is discretized individually by using Eq. (6) and a discrete mean curvature vector formula. Instead of doing that, in the present study, we use an integrated formula (31) derived in Appendix.

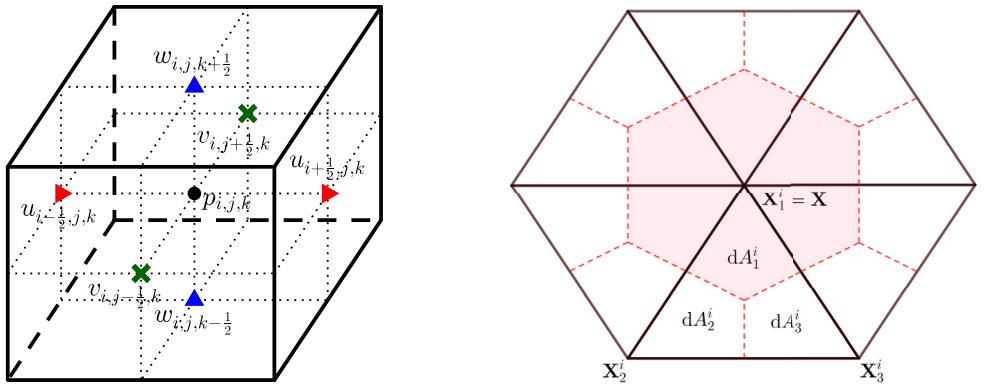

Fig. 1. In the left, a staggered grid scheme for fluid velocity (u, v, w) and fluid pressure p. In the right, an illustration of a 1-ring of triangles around a vertex $\mathbf{X} = \mathbf{X}_1^i$, and the effective area (colored in red) of the vertex $\mathbf{X}$ on triangulated closed interface. (For interpretation of the colors in the figure(s), the reader is referred to the web version of this article.)

3. Numerical scheme

The fluid variables are defined on the staggered grid in a computational cubic domain $\Omega = [a, b] \times [c, d] \times [e, f]$ as illustrated in the left of Fig. 1. The pressure p is defined at the cell center $\mathbf{x} = (x_i, y_i, z_i) = \big(a + (i - \frac{1}{2})\Delta x, c + (j - \frac{1}{2})\Delta y, e + (k - \frac{1}{2})\Delta z\big)$, where $i = 1, 2, \ldots, N_x$, $j = 1, 2, \ldots, N_y$, and $k = 1, 2, \ldots, N_z$. The velocity components u, v, and w are defined at cell-faces such as $(x_{i-\frac{1}{2}}, y_j, z_k)$, $(x_i, y_{j-\frac{1}{2}}, z_k)$, and $(x, y_j, z_{k-\frac{1}{2}})$, respectively. For convenience, we assume a uniform mesh grid size by $h = \Delta x = \Delta y = \Delta z$.

The incompressible interface immersed in fluid is approximated by a triangulated surface composed of the N_T-number of triangles and N_V-number of vertices correspondingly. The k-th vertex or marker is denoted by $\mathbf{X}_k$ for all $k \in \{1, 2, \ldots, N_V\}$ and the three vertices in the i-th triangle for all $i \in \{1, 2, \ldots, N_T\}$ are denoted by $\mathbf{X}_1^i$, $\mathbf{X}_2^i$, and $\mathbf{X}_3^i$. For each i-th triangle with three vertices $\mathbf{X}_i^1, \mathbf{X}_i^2$, and $\mathbf{X}_i^3$ associated with the k-th vertex, we always set by $\mathbf{X}_i^1 := \mathbf{X}_k$. The other two vertices $\mathbf{X}_2^i$ and $\mathbf{X}_3^i$ are labeled in the counter clockwise direction, so that the unit normal vector of the i-th triangle defined by $\mathbf{n}_i = \frac{(\mathbf{X}_2^i - \mathbf{X}_1^i) \times (\mathbf{X}_3^i - \mathbf{X}_1^i)}{\|(\mathbf{X}_2^i - \mathbf{X}_1^i) \times (\mathbf{X}_3^i - \mathbf{X}_1^i)\|_2}$ points into the outward direction of the surface. The triangular set denoted by $T(\mathbf{X}_k)$ consists of the triangles within the 1-ring surrounding $\mathbf{X}_k$, see the right of Fig. 1. On the i-th triangle in Fig. 1, the elastic tension is defined at the triangular center denoted by σ^i, and the triangular area is computed by

$$dA^i = \frac{1}{2} \|(\mathbf{X}_2^i - \mathbf{X}_1^i) \times (\mathbf{X}_3^i - \mathbf{X}_1^i)\|_2. \tag{9}$$

To solve the system described in Section 2, we discretize Eqs. (1)-(5) by the backward Euler (BE) scheme proposed in [20] for its 2D counterpart as

$$\frac{\mathbf{u}^{n+1}(\mathbf{x}) - \mathbf{u}^n(\mathbf{x})}{\Delta t} - \mu \Delta_h \mathbf{u}^{n+1}(\mathbf{x}) = -\nabla_h p^{n+1}(\mathbf{x}) + S_h^n[\sigma^{n+1}](\mathbf{x}) \quad \text{in } \Omega_h, \tag{10}$$

$$\nabla_h \cdot \mathbf{u}^{n+1}(\mathbf{x}) = 0 \quad \text{in } \Omega_h, \tag{11}$$

$$S_h^n[\sigma^{n+1}](\mathbf{x}) = \sum_{k=1}^{N_V} (\nabla_s \sigma^{n+1} - 2\sigma^{n+1} H^n \mathbf{n}^n)(\mathbf{X}_k^n)\, \delta_h(\mathbf{x} - \mathbf{X}_k^n)\, dA(\mathbf{X}_k^n), \tag{12}$$

$$\frac{\mathbf{X}_k^{n+1} - \mathbf{X}_k^n}{\Delta t} = \mathbf{U}_k^{n+1} := \widehat{S}_h^n[\mathbf{u}^{n+1}](\mathbf{X}^n) = \sum_{\mathbf{x}} \mathbf{u}^{n+1}(\mathbf{x})\, \delta_h(\mathbf{x} - \mathbf{X}_k^n) h^3 \quad \text{for all vertices } k, \tag{13}$$

$$\big(\nabla_{s_h} \cdot \mathbf{U}^{n+1}\big)^i = \big(\nabla_{s_h} \cdot \widehat{S}_h^n[\mathbf{u}^{n+1}](\mathbf{X}^n)\big)^i = 0 \quad \text{for all triangles } i. \tag{14}$$

The spatial operators ∇_h, $\nabla_h \cdot$ and Δ_h are the second-order central difference scheme of the gradient, the divergence, and the Laplacian defined on the staggered grid.

Referring to Eq. (31) derived in Appendix, the spreading operator (12) of elastic tension force is computed by

$$S_h^n[\sigma^{n+1}](\mathbf{x}) = \sum_{k=1}^{N_V} \mathbf{F}_\sigma(\mathbf{X}_k^n) dA(\mathbf{X}_k^n)\, \delta_h(\mathbf{x} - \mathbf{X}_k^n) = \sum_{k=1}^{N_V} \left(\sum_{i \in T(\mathbf{X}_k^n)} \frac{\sigma^{n+1,i}}{2} (\mathbf{X}_3^i - \mathbf{X}_2^i) \times \mathbf{n}_i \right) \delta_h(\mathbf{x} - \mathbf{X}_k^n).$$

In this formulation, to efficiently compute the actual force of elastic tension at vertices, we sweep the triangles rather than finding the associated triangles within a 1-ring around the vertex $\mathbf{X}_k$. To do so, on the i-th triangle, we first compute

three terms $\frac{\sigma^{n+1,i}}{2}(\mathbf{X}_3^i - \mathbf{X}_2^i) \times \mathbf{n}_i$, $\frac{\sigma^{n+1,i}}{2}(\mathbf{X}_1^i - \mathbf{X}_3^i) \times \mathbf{n}_i$, and $\frac{\sigma^{n+1,i}}{2}(\mathbf{X}_2^i - \mathbf{X}_1^i) \times \mathbf{n}_i$. Then these values contribute to the associated vertices $\mathbf{X}_1^i$, $\mathbf{X}_2^i$, and $\mathbf{X}_3^i$. Summing up those terms at each vertex, computing of tension force defined at vertices is accomplished.

In Eq. (13), the Lagrangian velocity $\mathbf{U}^{n+1}$ at vertex is interpolated by $\widehat{S}_h^n$ from its corresponding Eulerian velocity $\mathbf{u}^{n+1}$. The discrete surface divergence operator (14) defined on the i-th triangle (omitting the superscript time level index $n+1$) is computed by

$$\left(\nabla_{s_h} \cdot \mathbf{U}\right)^i = \frac{1}{2\,\mathrm{d}A^i}\left[\left((\mathbf{X}_3^i - \mathbf{X}_1^i) \times \mathbf{n}_i\right) \cdot (\mathbf{U}_2^i - \mathbf{U}_1^i) + \left(\mathbf{n}_i \times (\mathbf{X}_2^i - \mathbf{X}_1^i)\right) \cdot (\mathbf{U}_3^i - \mathbf{U}_1^i)\right],$$

through a discrete analogue of Eq. (8). The term $\mathbf{U}_j^i$ denotes the velocity $\mathbf{U}^{n+1}$ at the vertex $\mathbf{X}_j^i$.

For the discrete delta function defined by $\delta_h(\mathbf{x}) = \frac{1}{h^3}\phi\left(\frac{x}{h}\right)\phi\left(\frac{y}{h}\right)\phi\left(\frac{z}{h}\right)$, we employ

$$\phi(r) = \begin{cases} \frac{3}{8} + \frac{\pi}{32} - \frac{|r|^2}{4}, & |r| \le \frac{1}{2}, \\ \frac{1}{4} + \frac{1-|r|}{8}\sqrt{-2 + 8|r| - 4|r|^2} - \frac{1}{8}\arcsin\left(\sqrt{2}(|r|-1)\right), & \frac{1}{2} < |r| \le \frac{3}{2}, \\ \frac{17}{16} - \frac{\pi}{64} - \frac{3|r|}{4} + \frac{|r|^2}{8} + \frac{|r|-2}{16}\sqrt{-14 + 16|r| - 4|r|^2} & \\ \quad + \frac{1}{16}\arcsin\left(\sqrt{2}(|r|-2)\right), & \frac{3}{2} < |r| \le \frac{5}{2}, \\ 0, & \text{otherwise.} \end{cases} \tag{15}$$

This smoothed 4-point piecewise function is developed in [35].

3.1. Immersed boundary projection method

In this subsection, we provide a projection-based algorithm which efficiently solves the above system satisfying two constraints (11) and (14) simultaneously. To solve Eq. (10), we use an approximate fractional step method which decomposes Eq. (10) into two steps as in [23]

$$\frac{\mathbf{u}^* - \mathbf{u}^n}{\Delta t} - \mu\Delta_h\mathbf{u}^* = -\nabla_h p^n + S_h^n[\sigma^n], \tag{16}$$

$$\frac{\mathbf{u}^{n+1} - \mathbf{u}^*}{\Delta t} = -\nabla_h \delta p + S_h^n[\delta\sigma], \tag{17}$$

where we define

$$p^{n+1} = p^n + \delta p \quad \text{and} \quad \sigma^{n+1} = \sigma^n + \delta\sigma. \tag{18}$$

By comparing Eqs. (16)-(17) and Eq. (10), one can see that the exact form of pressure gradient should be $\nabla_h p^{n+1} = \nabla_h(p^n + \delta p) - \mu\Delta t(\Delta_h\nabla_h\delta p - \Delta_h S_h^n[\delta\sigma])$. However, to take the linear update of pressure and elastic tension into account, we neglect the last term which is an $O(\Delta t)$ splitting error of the discrete momentum equation. In the first step of Eq. (16), the viscous term is treated implicitly, thus our scheme without a penalization term is stable as long as the time step size Δt satisfies the usual CFL condition of the form $\Delta t \le Ch/\|\mathbf{u}\|_\infty$, where C is some constant less than one. In latter practical simulations, we choose the time step size $\Delta t = O(h)$. As known, the IB method is first-order accurate due to the delta function singularity discretization. It is not a limitation for the present scheme to use a second-order time discretization but it just does not help the overall accuracy significantly and makes the numerical scheme more complicated. So in this paper, we simply use the first-order backward Euler method in time discretization.

Here our goal is to find the solution variables at the $(n+1)$-th time level from given solutions at the n-th time level. The intermediate velocity $\mathbf{u}^*$ is easily obtained by solving Eq. (16) using FFT-based Helmholtz solver. Let us introduce an intermediate scalar field δp^* defined by

$$\delta p^* = \delta p - \Delta_h^{-1}\nabla_h \cdot S_h^n[\delta\sigma]. \tag{19}$$

By applying $\nabla_h\cdot$ and $\nabla_{s_h}\cdot\widehat{S}_h^n$ to Eq. (17) respectively, we obtain

$$\begin{aligned} &\frac{\nabla_h\cdot\mathbf{u}^{n+1} - \nabla_h\cdot\mathbf{u}^*}{\Delta t} = -\Delta_h\delta p + \nabla_h\cdot S_h^n[\delta\sigma] := -\Delta_h\delta p^*, \\ &\frac{\nabla_{s_h}\cdot\widehat{S}_h^n[\mathbf{u}^{n+1}] - \nabla_{s_h}\cdot\widehat{S}_h^n[\mathbf{u}^*]}{\Delta t} = -\nabla_{s_h}\cdot\widehat{S}_h^n[\nabla_h\delta p] + \nabla_{s_h}\cdot\widehat{S}_h^n[S_h^n[\delta\sigma]]. \end{aligned} \tag{20}$$

Using the two constraints $\nabla_h\cdot\mathbf{u}^{n+1} = 0$ in Eq. (11) and $\nabla_{s_h}\cdot\widehat{S}_h^n[\mathbf{u}^{n+1}] = \nabla_{s_h}\cdot\mathbf{U}^{n+1} = 0$ in Eq. (14), we have

$$\frac{\nabla_h \cdot \mathbf{u}^*}{\Delta t} = \Delta_h \delta p^*, \tag{21}$$

$$\frac{\nabla_{s_h} \cdot \mathbf{U}^*}{\Delta t} = \nabla_{s_h} \cdot \widehat{S}_h^n[\nabla_h \delta p] - \nabla_{s_h} \cdot \widehat{S}_h^n[S_h^n[\delta\sigma]]. \tag{22}$$

In the present projection step Eq. (17), one can immediately see that the pressure increment δp satisfies the zero Neumann boundary condition by directly multiplying the boundary normal to Eq. (17) and enforcing the same boundary condition on the velocities $\mathbf{u}^{n+1}$ and $\mathbf{u}^*$. (Notice that, the spreading term $S_h^n[\delta\sigma]$ in Eq. (17) has no effect since the value vanishes at the fluid domain boundary.) Therefore, by the definition of δp^* in Eq. (19), the boundary condition of δp^* is chosen naturally as zero Neumann boundary condition which is same as that of δp. Now the term δp^* can be found by solving Eq. (21) with $\frac{\partial \delta p^*}{\partial \mathbf{n}} = 0$ on $\partial\Omega$. Once δp^* is found, by substituting δp in Eq. (19) into Eq. (22), we have

$$\frac{\nabla_{s_h} \cdot \mathbf{U}^*}{\Delta t} = \nabla_{s_h} \cdot \widehat{S}_h^n \left[\nabla_h \delta p^* + \nabla_h \Delta_h^{-1} \nabla_h \cdot S_h^n[\delta\sigma]\right] - \nabla_{s_h} \cdot \widehat{S}_h^n[S_h^n[\delta\sigma]]. \tag{23}$$

Thus, the equation involving elastic tension increment $\delta\sigma$ becomes

$$\nabla_{s_h} \cdot \widehat{S}_h^n \left[\nabla_h \Delta_h^{-1} \nabla_h \cdot S_h^n[\delta\sigma]\right] - \nabla_{s_h} \cdot \widehat{S}_h^n[S_h^n[\delta\sigma]] = \frac{\nabla_{s_h} \cdot \mathbf{U}^*}{\Delta t} - \nabla_{s_h} \cdot \widehat{S}_h^n[\nabla_h \delta p^*]. \tag{24}$$

One can solve the above equation by using GMRES iterative method with the obtained solutions $\mathbf{U}^*$ and δp^*. For stopping criterion of GMRES iterations, the tolerance of maximum norm error is set by h^2, where h is the fluid mesh width. Now with $\delta\sigma$ and δp^*, we can find δp by solving $\Delta_h \delta p = \Delta_h \delta p^* + \nabla_h \cdot S_h^n[\delta\sigma]$ with the zero-Neumann boundary condition. Once we obtain δp and $\delta\sigma$, the fluid velocity $\mathbf{u}^{n+1}$ can be found in Eq. (17). Then we can update p^{n+1} and σ^{n+1} according to Eq. (18).

In summary, the step-by-step procedure of our algorithm is as follows.

Step 1: In Eq. (16), find the intermediate velocity $\mathbf{u}^*$ with the boundary condition of $\mathbf{u}^{n+1}$ via FFT-based Helmholtz solver.
Step 2: In Eq. (21), find the intermediate pressure increment δp^* with the zero-Neumann boundary condition via FFT-based Poisson solver.
Step 3: In Eq. (24), find the elastic tension increment $\delta\sigma$ via GMRES method. (To improve the conservation of local interfacial area, solve Eq. (27) instead.)
Step 4: In Eq. (19), find the pressure increment δp with the zero-Neumann boundary condition by solving $\Delta_h \delta p = \Delta_h \delta p^* + \nabla_h \cdot S_h^n[\delta\sigma]$ via FFT-based Poisson solver.
Step 5: In Eq. (17), obtain the new velocity $\mathbf{u}^{n+1}$, and then compute the new Lagrangian markers $\mathbf{X}^{n+1}$ according to Eq. (13).

In [23], the two-dimensional IB projection method is developed to simultaneously satisfy the volume divergence-free (11) and the surface divergence-free (14) in discrete sense. One can also prove those two conditions by using the differential formulation. We start by rewriting Eq. (17) as $\mathbf{u}^{n+1} = \mathbf{u}^* + \Delta t(-\nabla_h \delta p + S_h^n[\delta\sigma])$. Taking the discrete divergence on both sides, we have

$$\begin{aligned}
&\nabla_h \cdot \mathbf{u}^{n+1} \\
&= \nabla_h \cdot \mathbf{u}^* + \Delta t \left(-\Delta_h \delta p + \nabla_h \cdot S_h^n[\delta\sigma]\right) \\
&= \Delta t \Delta_h \delta p^* + \Delta t \left(-\Delta_h \delta p + \nabla_h \cdot S_h^n[\delta\sigma]\right) \quad \text{(by Eq. (21))} \\
&= \Delta t \Delta_h \left(\delta p - \Delta_h^{-1} \nabla_h \cdot S_h^n[\delta\sigma]\right) + \Delta t \left(-\Delta_h \delta p + \nabla_h \cdot S_h^n[\delta\sigma]\right) \\
&\qquad \left(\text{by the definition of } \delta p^* \text{ in Eq. (19)}\right) \\
&= \Delta t \left(\Delta_h \delta p - \nabla_h \cdot S_h^n[\delta\sigma]\right) + \Delta t \left(-\Delta_h \delta p + \nabla_h \cdot S_h^n[\delta\sigma]\right) \quad \left(\text{by } \Delta_h \Delta_h^{-1} = I\right) \\
&= 0.
\end{aligned}$$

Similarly, taking the discrete surface divergence of $\mathbf{U}^{n+1}$ on Eq. (17), we obtain

$$\begin{aligned}
&\nabla_{s_h} \cdot \mathbf{U}^{n+1} := \nabla_{s_h} \cdot \widehat{S}_h^n[\mathbf{u}^{n+1}] \\
&= \nabla_{s_h} \cdot \mathbf{U}^* + \Delta t \left(-\nabla_{s_h} \cdot \widehat{S}_h^n[\nabla_h \delta p] + \nabla_{s_h} \cdot \widehat{S}_h^n[S_h^n[\delta\sigma]]\right) \\
&= \Delta t \left(\nabla_{s_h} \cdot \widehat{S}_h^n \left[\nabla_h \delta p^* + \nabla_h \Delta_h^{-1} \nabla_h \cdot S_h^n[\delta\sigma]\right] - \nabla_{s_h} \cdot \widehat{S}_h^n[S_h^n[\delta\sigma]]\right) \\
&\quad + \Delta t \left(-\nabla_{s_h} \cdot \widehat{S}_h^n[\nabla_h \delta p] + \nabla_{s_h} \cdot \widehat{S}_h^n[S_h^n[\delta\sigma]]\right) \quad \text{(by Eq. (23))} \\
&= \Delta t \left(\nabla_{s_h} \cdot \widehat{S}_h^n[\nabla_h \delta p] - \nabla_{s_h} \cdot \widehat{S}_h^n[S_h^n[\delta\sigma]]\right)
\end{aligned}$$

$$+ \Delta t \left(-\nabla_{s_h} \cdot \widehat{S}_h^n[\nabla_h \delta p] + \nabla_{s_h} \cdot \widehat{S}_h^n[S_h^n[\delta\sigma]]\right) \quad \text{(by the definition of } \delta p \text{ in Eq. (19))}$$
$$= 0.$$

3.2. Improved conservation of local surface area

Here we present an algorithm to enhance the conservation of the local surface area for long-time simulations. In Eq. (20), the surface incompressibility is enforced by using the discrete condition (14), which simply sets the discrete surface divergence of new interfacial velocity by zero. However in practical implementation, the errors of local and total surface areas will accumulate and increase as time goes on. It is due to both the spatial and temporal errors of the present numerical scheme.

In a level-set formulation [16], the elastic tension is split into a variable part and constant part, then the constant is used to conserve the total surface area. In the present IB formulation, it is able to track all the triangles and their corresponding areas, so we implement to conserve solely the individual triangular area, thereby the total surface area is automatically conserved. To effectively conserve the area of the i-th triangle at the n-th time level denoted by $\mathrm{d}A^{n,i}$, we introduce a penalty-like term newly defining Eq. (14) by

$$\left(\nabla_{s_h} \cdot \mathbf{U}^{n+1}\right)^i := \frac{\mathrm{d}A^{0,i}/\mathrm{d}A^{n,i} - 1}{\Delta t}, \tag{25}$$

which is an approximation of the relation $\nabla_s \cdot \mathbf{U} = \frac{1}{\mathrm{d}A}\frac{\partial}{\partial t}\mathrm{d}A$ derived in [30,28]. As a result, at each time step, the new triangular area $\mathrm{d}A^{n+1,i}$ is targeted by the initial triangular area $\mathrm{d}A^{0,i}$. So, dropping the index i for the convenience, Eq. (22) is modified to

$$\frac{\nabla_{s_h} \cdot \mathbf{U}^* - \frac{\mathrm{d}A^0/\mathrm{d}A^n - 1}{\Delta t}}{\Delta t} = \nabla_{s_h} \cdot \widehat{S}_h^n[\nabla_h \delta p] - \nabla_{s_h} \cdot \widehat{S}_h^n[S_h^n[\delta\sigma]]. \tag{26}$$

Therefore, instead of solving Eq. (24), we find $\delta\sigma$ by solving

$$\nabla_{s_h} \cdot \widehat{S}_h^n\left[\nabla_h \Delta_h^{-1} \nabla_h \cdot S_h^n[\delta\sigma]\right] - \nabla_{s_h} \cdot \widehat{S}_h^n[S_h^n[\delta\sigma]] = \frac{-\frac{\mathrm{d}A^0/\mathrm{d}A^n - 1}{\Delta t} + \nabla_{s_h} \cdot \mathbf{U}^*}{\Delta t} - \nabla_{s_h} \cdot \widehat{S}_h^n[\nabla_h \delta p^*]. \tag{27}$$

4. Numerical results

The initial incompressible closed interface is configured by the construction of an icosahedron, and then each triangle is refined by subdividing into four smaller triangles with half edge-length. The newly created vertices shall be projected onto the sphere, and we repeat this refinement process until the desired resolution is reached. We denote N_V by the number of vertices on the triangulated interface and N_T by the corresponding number of triangles. These two numbers are related by $N_T = 2(N_V - 2)$, and the number of edges N_E can be easily calculated by $N_E = 3N_T/2$ since two neighboring triangles share the same edge. Thus, one can easily derive the famous formula $N_V - N_E + N_T = 2$. Throughout the paper, we shall choose the surface grid number $(N_V, N_T) = (12, 20)$, $(42, 80)$, $(162, 320)$, $(642, 1280)$, and $(2562, 5120)$.

We introduce a dimensionless number called the reduced volume $v < 1$, representing the volume ratio between the given incompressible interface and the sphere with the same surface area. To obtain a prolate (or oblate) spheroid with the specific reduced volume v, we adjust the lengths of principal semi-axes. For all surfaces used here, we fix the enclosed volume by $4\pi/3$ so that the effective radius is 1. For instance, the prolate spheroid with $v = 0.95$ has the approximate lengths of principal semi-axes as $(1.355, 0.88, 0.88)$. Throughout this study, the fluid viscosity is chosen as $\mu = 1$. The computational domain size is set by $[-4, 4]^3$ and the fluid mesh width is by $h = 8/N$, where N is the grid number in each dimension. The time step size is set by $\Delta t = h/8$. In all the numerical experiments performed here, we adopt the improved conservation method presented in Subsection 3.2, and all the losses of local and total surface areas and the enclosed volume are less than about 2%, unless otherwise mentioned. To perform a simulation up to $t = 1$ for the case of $(N_V, N_T) = (2562, 5120)$ and $N = 128$, it takes about 15 hours to complete on a workstation equipped with a 3.7 GHz Intel Xeon E5-1630 CPU.

Before proceeding, we state the norm and the convergence rate used in this paper. For a scalar function f and a vector field $\mathbf{F}$ defined on interfacial vertices (or markers) $\mathbf{X}$, their L_2 norms are computed (under the fluid grid number N in each direction) by

$$\|f_{N_V,N}\|_2 = \left(\sum_{k=1}^{N_V} f^2(\mathbf{X}_k)\,\mathrm{d}A(\mathbf{X}_k)\right)^{1/2}, \quad \text{and}$$

$$\|\mathbf{F}_{N_V,N}\|_2 = \left(\sum_{k=1}^{N_V} \mathbf{F}(\mathbf{X}_k) \cdot \mathbf{F}(\mathbf{X}_k)\,\mathrm{d}A(\mathbf{X}_k)\right)^{1/2}, \quad \text{respectively.}$$

Table 1
At time $t = 2$, convergence analysis of the relative errors of the fluid velocity (u, v, w), the fluid pressure p, the position vector $\mathbf{X}$ of incompressible interface, and the elastic tension σ. In this test, the reference solution is obtained in the case of $(N_V, N) = (2562, 128)$.

N_V, N	$E_2^{N_V}(u)$	Rate	$E_2^{N_V}(v)$	Rate	$E_2^{N_V}(w)$	Rate
42, 16	8.869E-02	–	1.913E+00	–	1.755E+00	–
162, 32	2.852E-02	1.63	5.212E-01	1.87	5.020E-01	1.80
642, 64	2.603E-03	3.45	1.291E-01	2.01	1.259E-01	1.99
N_V, N	$E_2^{N_V}(p)$	Rate	$E_2^{N_V}(\mathbf{X})$	Rate	$E_2^{N_V}(\sigma)$	Rate
42, 16	8.942E-01	–	1.838E-01	–	2.749E+00	–
162, 32	4.570E-01	0.96	1.745E-02	3.39	9.334E-01	1.55
642, 64	1.377E-01	1.73	5.961E-03	1.54	3.743E-01	1.31

For a function defined on triangular facets, the norm at vertices is obtained by the area-weighted interpolation of the triangular values onto the vertices. The L_2 norm of a scalar function defined on fluid mesh grid is computed in a similar manner as

$$\|f_{N_V,N}\|_2 = \left(\sum_{k=1}^{N} \sum_{j=1}^{N} \sum_{i=1}^{N} f_{ijk}^2 h^3 \right)^{1/2}.$$

Now consider a triangulated interface approximated by N_V-number of vertices which is immersed in 3D domain composed of N^3-number of grid points. The relative error of an unknown function f on such interface between two successive grids is measured by

$$E_2^{N_V}(f) = \|f_{N_V,N} - f_e\|_2 / \|f_e\|_2, \tag{28}$$

where f_e is the known exact solution. When the solution is not known, we replace f_e by an interpolated numerical solution obtained in the most refined resolution. We use the notation $E_\infty^{N_V}(f)$ for the maximum relative error of f defined similarly as Eq. (28). Notice that the resolutions of the fluidic domain and interfacial domain are adjusted simultaneously. The rate of convergence is computed by

$$\text{Rate} = \log_2 \left(E_2^{N_V}(f) \big/ E_2^{N_V^r}(f) \right), \tag{29}$$

where $E_2^{N_V^r}(f)$ is the relative error at the next higher refinement level of surface grid N_V.

Throughout the paper, we compute the inclination angle θ and the angular velocity $\overline{\omega}$ of a suspended incompressible interface as follows. To measure θ, the evolving interface is fitted to an ellipsoid by least squares approximation, then θ is given by the angle between the x-axis and the longest axis of the interface. The angular velocity (or averaged tank-treading frequency) is obtained from

$$\overline{\omega} = \frac{1}{N_V} \sum_{k=1}^{N_V} \|\mathbf{r}_k \times \mathbf{V}_k\|_2 / \|\mathbf{r}_k\|_2^2,$$

where the position vector $\mathbf{r}_k$ of the marker (or vertex) and the marker velocity $\mathbf{V}_k$ are projected onto the xz-plane as in [28]. As seen, the average of tank-treading frequency is taken over all vertices. To avoid the computational singularity, the markers with $\|\mathbf{r}_k\|_2 < 10^{-3}$ are excluded in computing $\overline{\omega}$.

4.1. Convergence study under shear flow

We first check the convergence rate of our numerical method proposed in Section 3. We put an incompressible interface under shear flow $\mathbf{u} = (z, 0, 0)$. Fig. 2 illustrates the temporal evolution of interfacial deformations for the case of reduced volume $v = 0.95$ in three different resolutions of $(N_V, N) = (162, 32)$, $(642, 64)$, and $(2562, 128)$. In the figure, the interfacial shapes and the inclination angles at $t = 1$ and 2 appear to coincide with each other so the interfaces undergo the steady tank-treading motion.

Table 1 shows the convergence rates of all the solution variables at time $t = 2$. The rates of fluid velocity components (u, v, w) show better than first-order accuracy. A theoretical study in [6] suggests that the IB method using smoothed delta function has half-order accuracy for the fluid pressure p, but our result shows higher accuracy. The convergence behavior of the position vector $\mathbf{X}$ is analogous to the 2D result obtained in literature [23]. The elastic tension σ has first-order accuracy as well. The present results show better accuracy than anticipated probably due to steady behavior at $t = 2$.

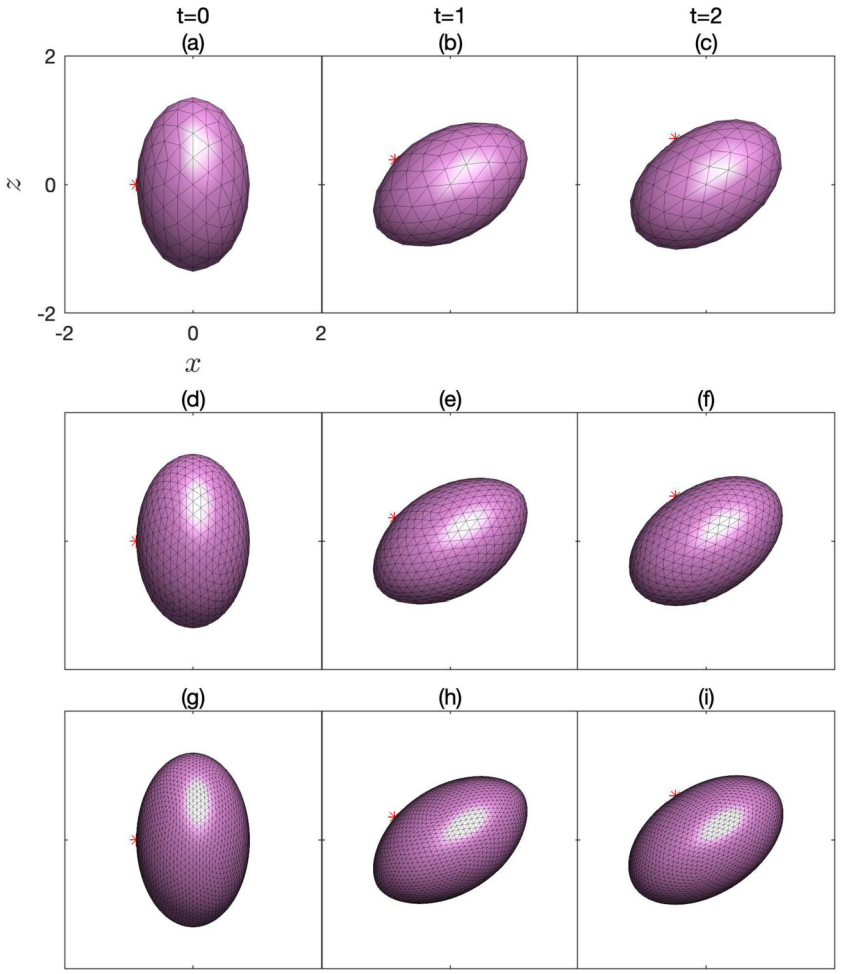

Fig. 2. Under shear flow, the snapshots of initially prolate interface at $t = 0, 1, 2$. The reduced volume is fixed by $v = 0.95$ and the resolution (N_V, N) is (a-c) $(162, 32)$; (d-f) $(642, 64)$; (g-i) $(2562, 128)$. The whole computational domain is $[-4, 4]^3$.

Table 2
At time $t = 2$, convergence analysis of the relative errors of the local surface area $\mathrm{d}A$, the total surface area A, and the enclosed volume V of interface.

N_V, N	$E_\infty^{N_V}(\mathrm{d}A)$	Rate	$E_\infty^{N_V}(A)$	Rate	$E_\infty^{N_V}(V)$	Rate
42, 16	7.982E-04	–	4.296E-04	–	3.478E-02	–
162, 32	3.216E-04	1.31	1.349E-04	1.67	9.559E-03	1.86
642, 64	1.028E-04	1.64	3.647E-05	1.88	5.004E-03	0.93
2562, 128	2.746E-05	1.90	9.239E-06	1.98	2.614E-03	0.93

In the present study of an incompressible interface using the IB projection method, one of the major issues is to check the numerical behaviors of the local surface area $\mathrm{d}A$, the total surface area A, and the enclosed volume V of the interface. Fig. 3 shows the temporal evolution of relative errors of three quantities, and its corresponding convergence analysis at time $t = 2$ is provided in Table 2. Due to the surface incompressibility property, the values for local surface area $\mathrm{d}A$ and the total surface area A should remain the same as the initial ones. One can see from Fig. 3, the relative errors for both values are within $O(10^{-4})$ as time evolves which shows the effectiveness of the local surface area conservation technique described in Subsection 3.2. Meanwhile, second-order accuracies of these two quantities is also verified in Table 2. This is due to the penalty-like term $\frac{\mathrm{d}A^0/\mathrm{d}A^n - 1}{\Delta t^2}$ in Eq. (26), where the term $1/\Delta t^2$ acts as a penalty parameter. To illustrate the effectiveness of the present improved conservation of the local surface area, we also compare some related results later in Subsection 4.2. Unlike the local and total surface areas, the relative error of the enclosed volume V increases as time goes as expected in the IB method if no extra mechanism is applied. The volume conservation has first-order accuracy. In Subsection 4.4, a similar penalty-like technique will also be applied to conserve the volume when the bending effect is considered.

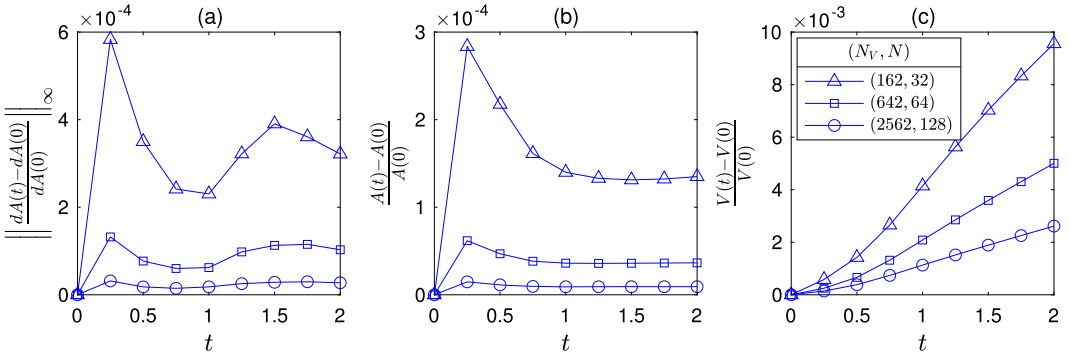

Fig. 3. The temporal evolution of the relative errors of (a) local surface area dA in L_∞ norm; (b) total surface area A; (c) enclosed volume V of interface.

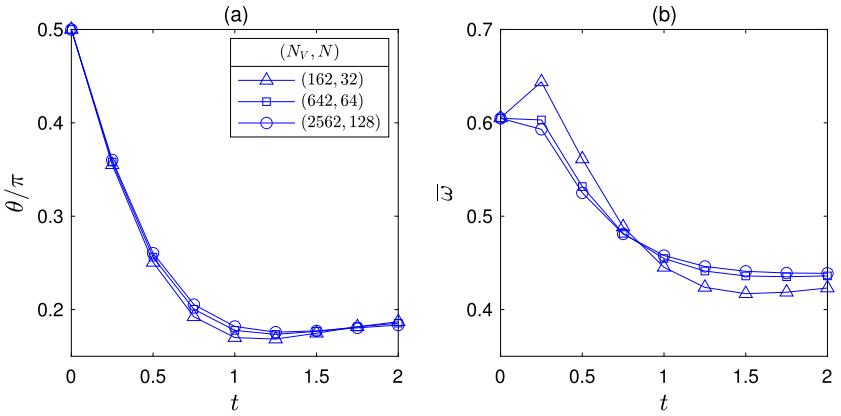

Fig. 4. The temporal evolution of (a) the inclination angle θ; (b) the averaged tank-treading frequency $\overline{\omega}$.

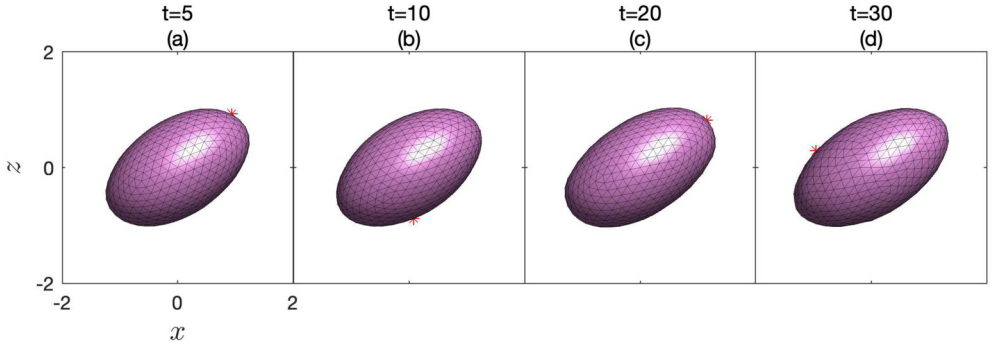

Fig. 5. Under shear flow, the snapshots of initially prolate interface at $t = 5, 10, 20$, and 30. This corresponds to Fig. 2(d-f). The reduced volume is fixed by $v = 0.95$ and the resolution is $(N_V, N) = (642, 64)$.

In addition to the solution variable results given above, Fig. 4 provides the physical quantitative results, such as the inclination angle θ/π and the averaged tank-treading frequency $\overline{\omega}$ as functions of time. The three plots in each quantity begin to converge to a constant at about $t = 1$ and agree well with each other. The present result is consistent with the quantitative results observed in Fig. 2.

In the above shear-induced deformation problem, one may wonder whether an evolving interface reaches a steady tank-treading motion. In Fig. 5, we show a simulation result obtained up to $t = 30$. The numerical setup corresponds to the case shown in Fig. 2(d-f). This simulation result indicates that the steady state is achieved at early time (about $t = 1$) and then the interface continues to tank-tread without changing the shape. The quantitative results associated with the inclination angle and the angular velocity shown in Fig. 4 also identify the onset of steady state.

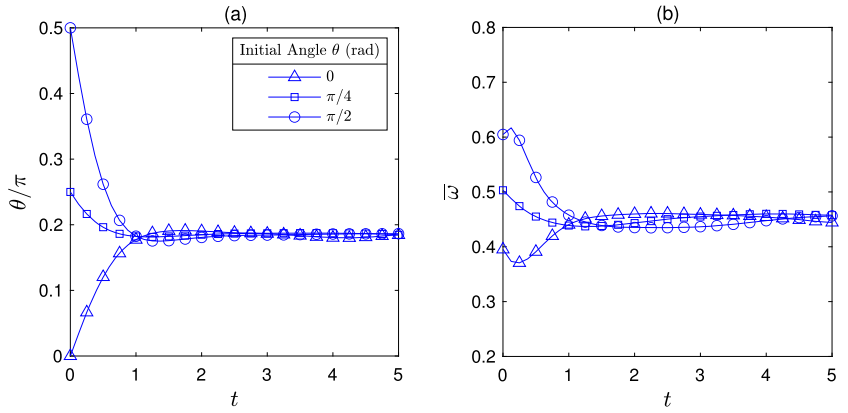

Fig. 6. For different inclination angles at initial time, the temporal evolution of (a) the inclination angle θ; (b) the averaged tank-treading frequency $\overline{\omega}$. The reduced volume is fixed by $\nu = 0.95$.

4.2. Effect of different reduced volumes

Before studying the effect of various reduced volumes ν, we first study the effect of the initial configuration of the incompressible prolate interface, for which three different initial angles are tested. We initially put the prolate interface with $\nu = 0.95$ tilted by $\theta_0 = 0$, $\pi/4$, and $\pi/2$, then measure the temporal evolution of inclination angle θ and averaged tank-treading frequency $\overline{\omega}$. In Fig. 6, these two quantities describing the interfacial state tend to converge to the respective constant values at about $t = 1$. This implies that the dynamics of the incompressible interface under shear flow is nearly independent of its initial angle θ, so we simply fix by $\theta_0 = \pi/2$ for initial configuration.

To study the effect of various ν on shear-induced dynamics, we show the temporal evolution of interfacial deformations in Fig. 7 for $t = 0$, 2.5, 5 and $\nu = 0.975$, 0.9, 0.8, 0.7. For all cases performed here, the initial configurations are prolate spheroidal, and they undergo a steady tank-treading motion tilted by about $\pi/4$ or lower angle. As seen, the interfacial inclination angle at $t = 5$ gets lower as ν decreases. On the interfaces, the red-colored asterisk '$*$' indicates a tracing marker, so one can see that the interfacial speed in tank-treading motion gets slower with decreasing ν. The whole shape of incompressible interfaces with small ν even deviates some extent from the ellipsoid. In particular, Fig. 7(i) exhibits an *S*-like shape which is consistent with the observation in experiment [21]. As shown in Fig. 7(l), the shape for smaller $\nu = 0.7$ shows a similar trend.

Fig. 8 shows the distribution of elastic tension σ on steady-state interfaces for different ν, post-processed using an efficient filtering method [10, Eq. (17)]. As in the 2D case [23], for all tests performed here, the value of σ nearby two tips coinciding with the inclination angle appears to be lower than the rest of the interface. Contrary to the role of a negative pressure gradient, the tangential force $\nabla_s \sigma$ acts in the direction from a lower tension toward a higher one. Thus, it is reasonable that a smaller value of σ around the tips generates the tangential force which acts in the opposite direction of the interfacial elongation. Higher values of σ are distributed in the middle of the interface due to the shear-driven flow topology.

To carefully check the interfacial state for various ν, the temporal evolution of two quantities, the inclination angle θ/π and the averaged tank-treading frequency $\overline{\omega}$, are shown in Fig. 9(a, b). In this test, we also check the effect of improved conservation of local surface area presented in Subsection 3.2. The results in the blue colored solid lines are obtained without using the conservation method, whereas those in the red colored dotted lines are obtained by using the method. For both quantities in the figures, regardless of the usage of conservation method, all the plots tend to converge, so we can conclude that the incompressible interfaces at time $t = 5$ undergo the tank-treading motion in the steady state. Meanwhile, both groups of the results agree well to each other, even though the conservation of local and total surface areas are dramatically improved as shown in Fig. 9(c, d). The relative errors of the quantities dA and A are bounded above by 2×10^{-4} and 2×10^{-5} respectively, and they tend to remain constant with time. This indicates that the algorithm proposed in Subsection 3.2 preserves the area of every single triangle, hence the total surface area well. Simultaneously, the physics of the incompressible interface is essentially unaltered and preserved for long-time simulations.

To further verify that our method correctly simulates physical problems, two quantities θ and $\overline{\omega}$ mentioned above are also compared with some previous results in literature. Fig. 10 shows our result of both quantities as functions of ν in comparison with theoretical analysis [13,17], experimental result [37], and penalty-based immersed boundary (pIB) method [28]. The numerical result of a vesicle with bending modulus $\chi = 100$ is chosen in the pIB method since large χ implies a minor effect of bending force. When the fluid viscosity is set by $\mu = 1$, our result for θ is in good agreement with other results, while for $\overline{\omega}$, it agrees well only when $\nu \geq 0.8$. In particular, in Fig. 10(b), the tank-treading frequencies for $\nu < 0.8$ deviate significantly from the theoretical prediction. As seen in the case of larger viscosities $\mu = 10$ and 100 using our method, we can see that $\overline{\omega}$ for small ν gets closer to the theoretical result as μ increases, while the inclination angle is

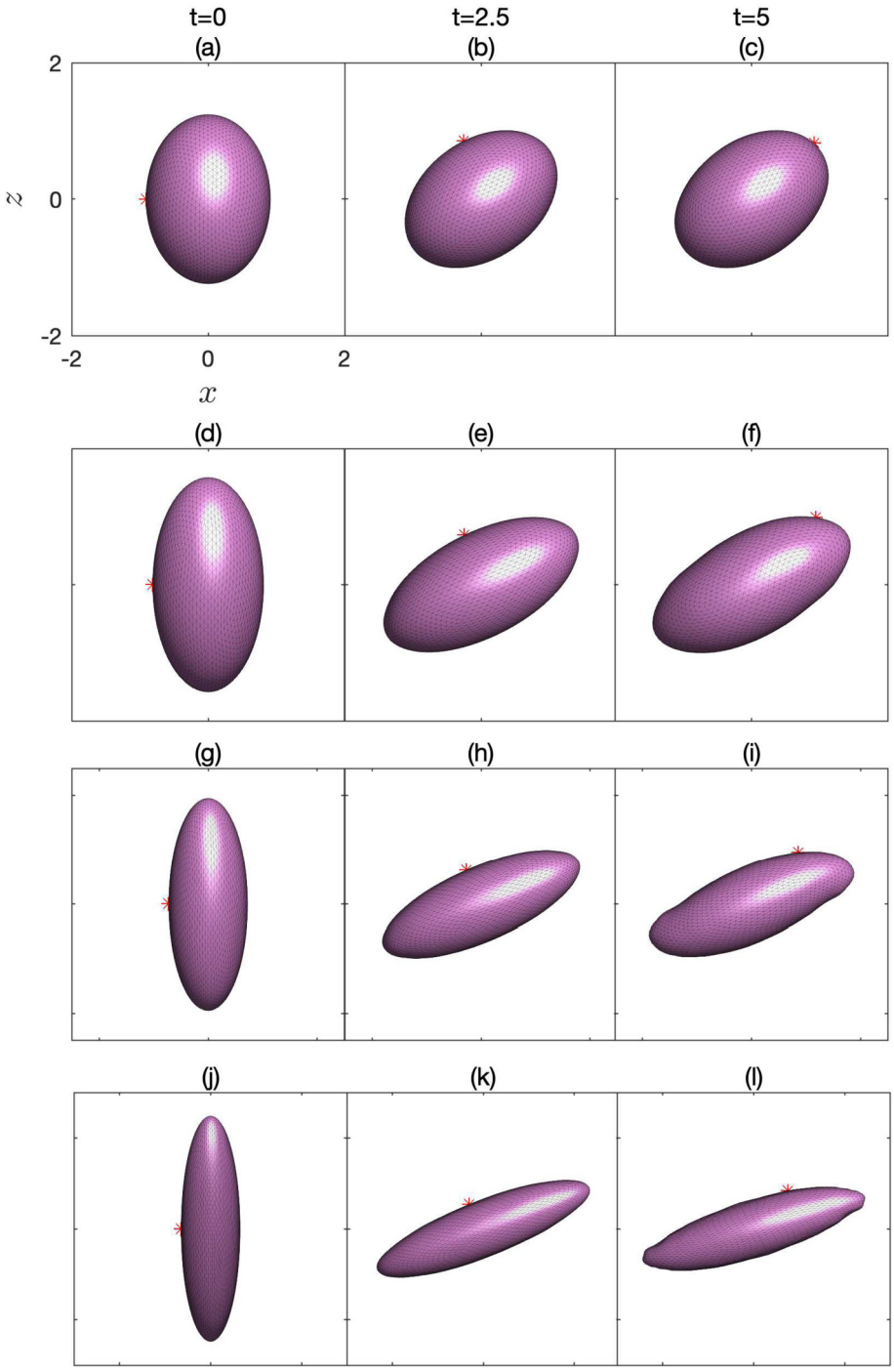

Fig. 7. Under shear flow, the snapshots of initially prolate interface at $t = 0, 2.5, 5$, where the reduced volume ν is (a-c) 0.975; (d-f) 0.9; (g-i) 0.8; (j-l) 0.7. The whole computational domain is $[-4, 4]^3$.

still unaffected. So it is apparent that the discrepancy of $\overline{\omega}$ for small ν originates from the effect of fluid viscosity μ. This conclusion is indeed consistent with the fact that the theoretical result assumes a very viscid fluid.

4.3. Initially oblate interface under shear flow

So far, we have considered only a prolate interface at the initial time. We now set an oblate interface initially and show its dynamics in Fig. 11. The oblate spheroid with $\nu = 0.9$ employed here has the approximate length of principal semi-axes

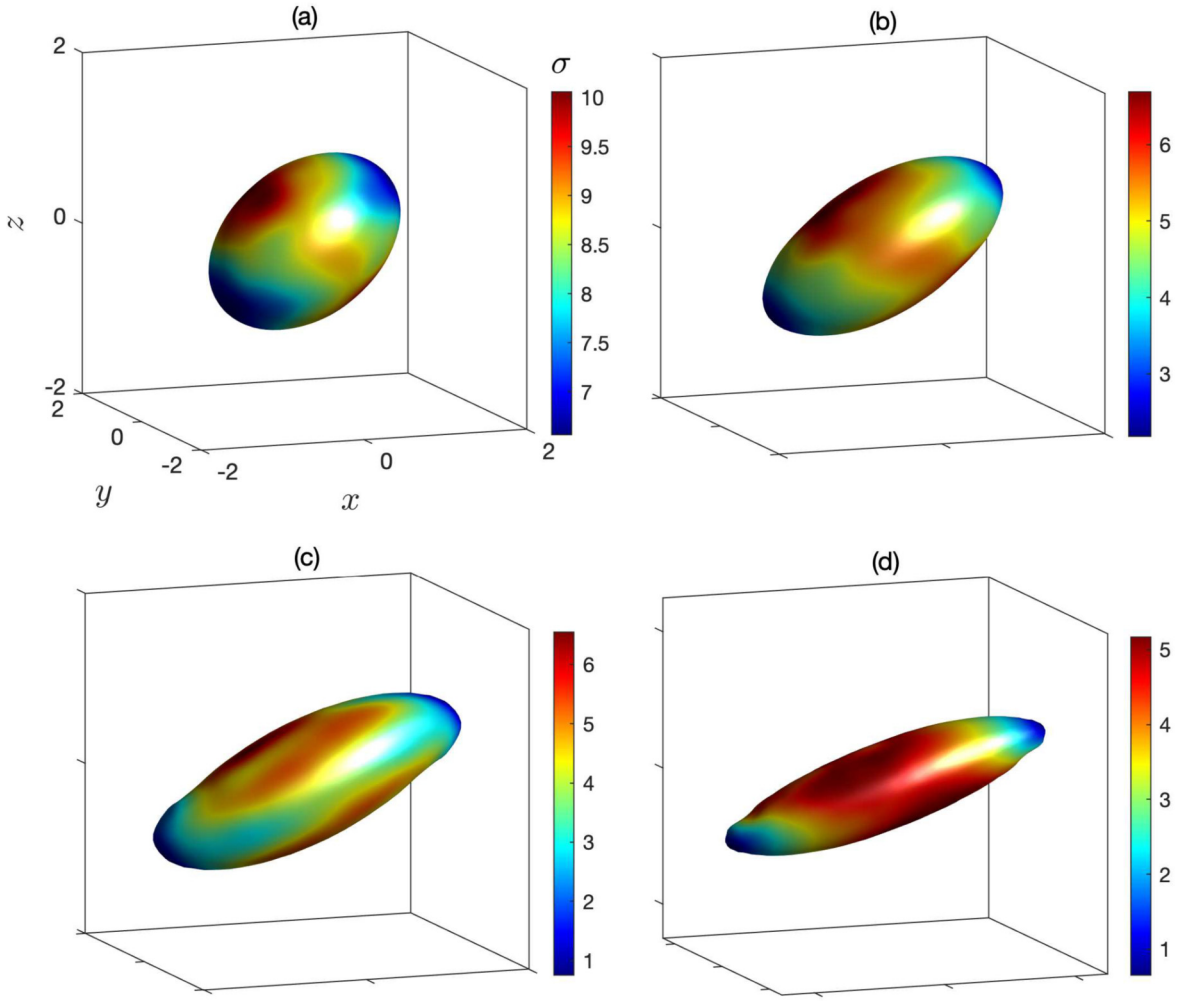

Fig. 8. The color distribution of elastic tension σ on prolate interface at $t = 5$, where the reduced volume v is (a) 0.975; (b) 0.9; (c) 0.8; (d) 0.7. These correspond to Fig. 7(c, f, i, l), respectively.

as $(1.23, 1.23, 0.68)$. Unlike the red blood cells [3,8], there is no extra interfacial force other than the elastic tension force caused by the surface incompressibility in the present study. So the initial oblate interface eventually transforms into a prolate one as shown in Fig. 11(f). One can compare this transition with Fig. 7(d-f). As one can expect, although not shown here, the shear-induced deformation of initially oblate interface with small v produces a significant distortion of a triangular mesh, so the mesh control or remeshing is necessary especially for simulating thinner and elongated interfaces. We leave this for future work.

4.4. Vesicle deformation with improved volume conservation

To show the applicability of our method, we add the Helfrich-type bending force $\mathbf{F}_b$ [11] into the model to simulate more realistic vesicle problem case. Furthermore, to improve the enclosed volume conservation, we add an extra penalty force $\mathbf{F}_v$ into the model so the momentum equation (1) becomes

$$\frac{\partial \mathbf{u}}{\partial t} + \nabla p = \mu \Delta \mathbf{u} + S[\sigma] + \int_\Gamma (\mathbf{F}_b + \mathbf{F}_v)\, \delta(\mathbf{x} - \mathbf{X}(\alpha, \beta, t))\, \mathrm{d}A,$$

where

$$\mathbf{F}_b = \frac{c_b}{2}\left(\Delta_s H + 2H(H^2 - K)\right)\mathbf{n},$$
$$\mathbf{F}_v = -c_v \frac{V(t) - V(0)}{V(0)}\mathbf{n}. \tag{30}$$

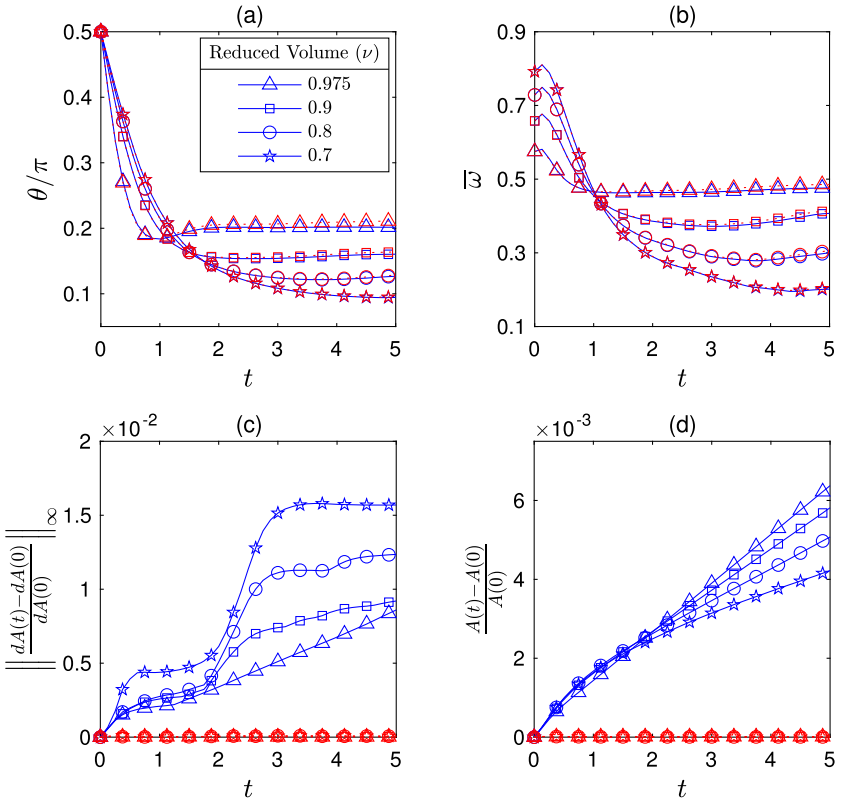

Fig. 9. For initially prolate interface with different reduced volumes ν, the temporal evolution of (a) the inclination angle θ; (b) the averaged tank-treading frequency $\overline{\omega}$; (c) the relative error of local surface area dA in L_∞ norm; (d) the relative error of total surface area A. The solid lines (colored in blue) indicate no usage of improved local area conservation method, whereas the dotted lines (colored in red) indicate the usage of the method.

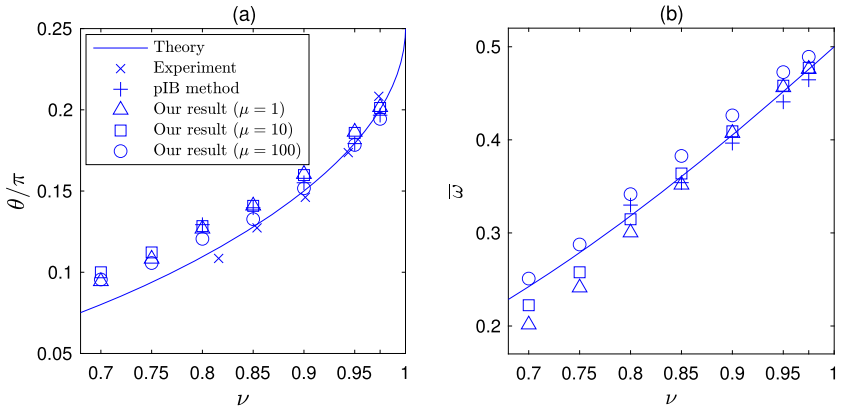

Fig. 10. For initially prolate interface with different reduced volumes ν, the comparison of (a) the inclination angle θ; (b) the averaged tank-treading frequency $\overline{\omega}$ at time $t = 5$.

Here c_b is the bending rigidity, c_v is the penalty parameter, Δ_s is the Laplace-Beltrami operator, and K is the Gaussian curvature. The penalty force $\mathbf{F}_v$ for improved volume conservation as a feedback mechanism is ideally consistent with the fluid incompressibility. For structure-interaction problems, this force is widely used particularly for grid-based numerical methods such as in [36,16]. The penalty parameter c_v should be carefully chosen so that the volume loss is well-controlled during simulations. From our previous numerical experiences, the stiffness caused by this extra force addition is problem-dependent. Since the shape of interface does not change dramatically from step to step, the stiffness is not significant as the time step size in present simulations can be chosen as $\Delta t = O(h)$.

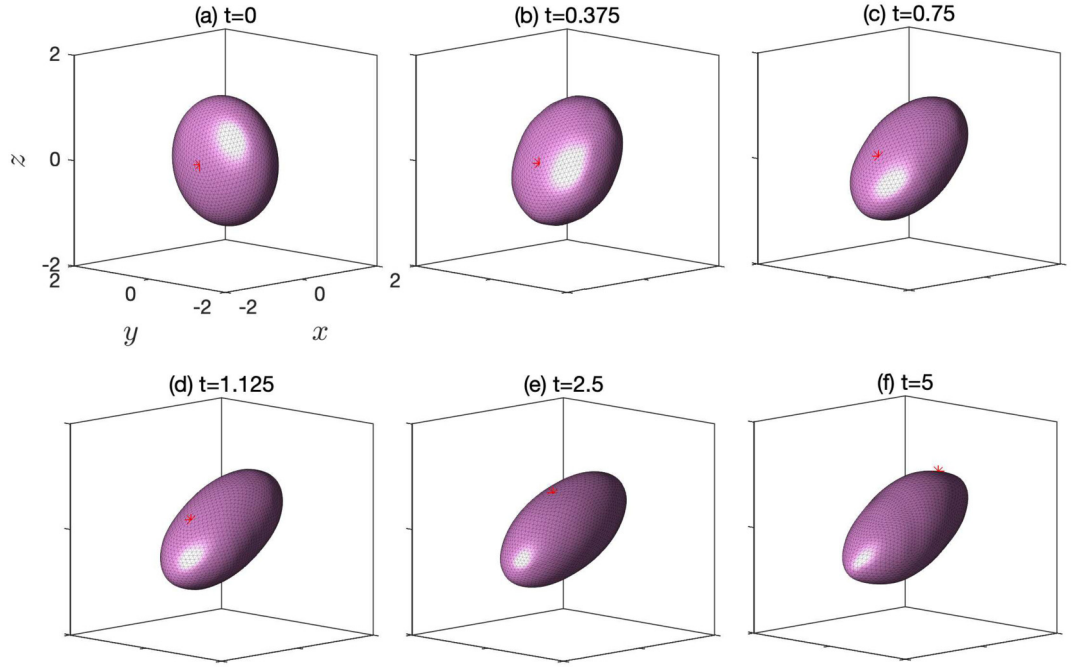

Fig. 11. Under shear flow, the snapshots of initially oblate interface at some chosen times, where the reduced volume is fixed by $v = 0.9$. This is the counterpart of the initially prolate interface shown in Fig. 7(d-f). The whole computational domain is $[-4, 4]^3$.

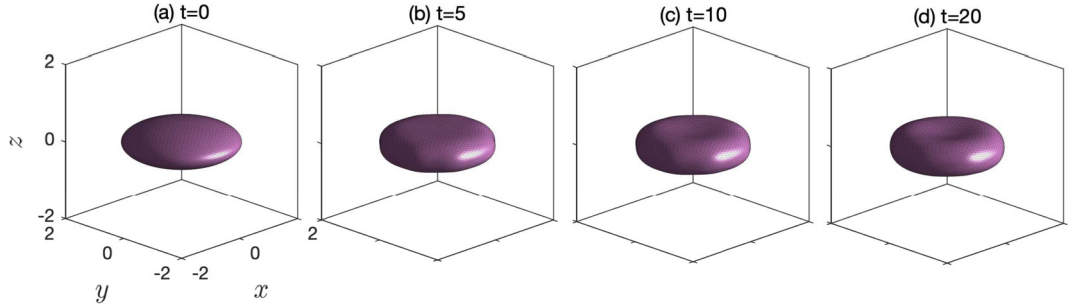

Fig. 12. Under quiescent flow, the snapshots of initially oblate vesicle at some chosen times, where the reduced volume is fixed by $v = 0.7$. The whole computational domain is $[-4, 4]^3$.

In the present IB projection method, the above two interfacial forces are discretized explicitly in Eq. (16), so we have

$$\frac{\mathbf{u}^* - \mathbf{u}^n}{\Delta t} - \mu \Delta_h \mathbf{u}^* = -\nabla_h p^n + S_h^n[\sigma^n] + \sum_{k=1}^{N_V} \left[\mathbf{F}_b(\mathbf{X}_k^n) + \mathbf{F}_v(\mathbf{X}_k^n))\right] \delta_h(\mathbf{x} - \mathbf{X}_k^n)\, \mathrm{d}A(\mathbf{X}_k^n).$$

Note that, we use the discrete bending force proposed in [34]. Due to the complicated form of the bending force $\mathbf{F}_b$, most of three-dimensional numerical methods in literature [17,4,36,15,16,34] treat the term explicitly. One may wonder that the explicit treatment of $\mathbf{F}_b$ will increase the stiffness of time discretization. Fortunately, the typical vesicle bending modulus c_b is small enough so the influence of the bending force stiffness is in fact not severe as you can see that our choice of time step size in simulations is about $\Delta t = O(h)$.

For our test of vesicle relaxation, the bending rigidity is set by $c_b = 0.1$, and the penalty parameter is by $c_v = 10^5$. The improved conservation of local surface area presented in Subsection 3.2 is also adopted. We put an initially oblate vesicle with $v = 0.7$ whose approximate lengths of principal semi-axes are $(1.47, 1.47, 0.483)$ in quiescent flow. As expected, the vesicle in Fig. 12 deforms to a biconcave shape which is the typical shape of red blood cells. A similar experiment was also shown in [28, Fig. 7]. One can further incorporate the convection term $(\mathbf{u} \cdot \nabla)\mathbf{u}$ which enables to give the inertia effect to the vesicle dynamics, but we ignore it here.

In Fig. 13, three quantities associated with the surface area and the enclosed volume of the vesicle are drawn in terms of time. The evolution of relative errors of $\mathrm{d}A$ and A indicates that the vesicle tends to reach a steady state at about $t = 10$. Even in the equilibrium state, the bending force still acts on the vesicle interface. So, although omitted here, the volume loss

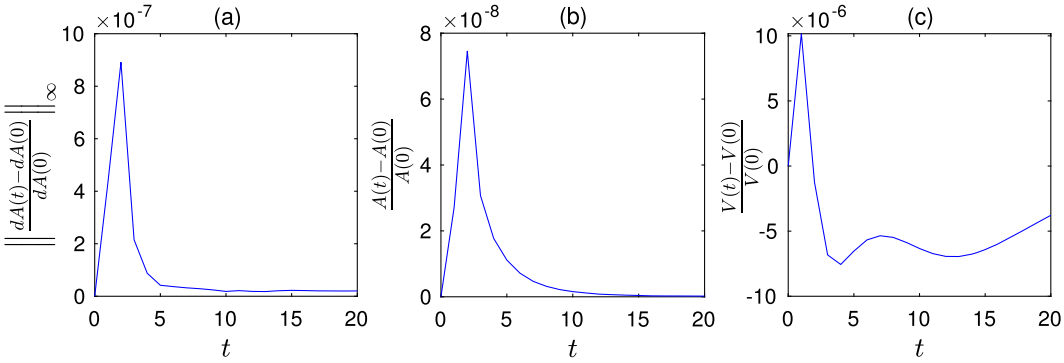

Fig. 13. With the improved volume conservation ($c_v = 10^5$ in Eq. (30)), the temporal evolution of the relative errors of (a) local surface area dA in L_∞ norm; (b) total surface area A; (c) enclosed volume V of vesicle. This corresponds to Fig. 12.

increases to about 10^{-4} with time when the volume conservation force $\mathbf{F}_v$ is not imposed; that is, $c_v = 0$ in Eq. (30). On the other hand, by setting $c_v = 10^5$ in $\mathbf{F}_v$, the volume conservation is significantly improved as shown in Fig. 13(c). In the presence of these improved conservation methods both for dA and V, the magnitudes of the relative error of local interface area dA, total interface area A, and the enclosed volume V at $t = 20$ are 2.03×10^{-8}, 1.99×10^{-10}, and 3.78×10^{-6}, respectively. This implies that our method employing Eqs. (25) and (30) conserves well for these quantities and is suitable for long-time simulations of vesicle dynamics.

5. Conclusion

For simulating 3D incompressible interface in unsteady Stokes flow, we have extended the 2D immersed boundary (IB) projection method proposed in the previous paper [23] to three dimensions. The incompressible interface as a prototype of the vesicle membrane is discretized by a triangulation. The unknown elastic tension is defined on triangles so that the elastic tension force is computed at the vertices or Lagrangian markers. On the triangulated interface, a simple and energy-consistent formula for computing the tension force is derived, and a direct discretization of surface divergence operator is developed as well.

In the spirit of projection method, the fluid pressure and the elastic tension as Lagrange multipliers are obtained by efficiently solving individual equation under the corresponding local volumetric and interfacial incompressibilities. By introducing an intermediate pressure increment, we are able to ensure both constraints simultaneously. We further propose a newly defined discrete operator of surface divergence of interfacial velocity. This remedy allows to perform long-time simulations by improving the conservation of the local interfacial area. To verify our method, we investigate the convergence analysis of the solution variables defined on fluid and interface in shear-induced deformations. The effect of initial configuration of an incompressible interface is extensively studied under shear flow. To show the applicability of our method, an oblate vesicle in quiescent flow has been simulated by incorporating with bending resistance and improved volume conservation.

For future work, a different representation of incompressible interface such as spherical harmonics should be able to compute the surface operators more accurately. The application of our method to realistic biological problems is also a promising subject for further study. Meanwhile, it will be interesting to couple with remeshing, or even adaptive mesh refinement to achieve a better quality of interfacial mesh control.

CRediT authorship contribution statement

Kian Chuan Ong: Conceptualization, Methodology, Validation, Visualization. **Ming-Chih Lai:** Funding acquisition, Supervision, Writing – review & editing. **Yunchang Seol:** Formal analysis, Investigation, Software, Writing – original draft.

Declaration of competing interest

The authors declare that they have no known competing financial interests or personal relationships that could have appeared to influence the work reported in this paper.

Acknowledgement

The work of M.-C. Lai was supported in part by Ministry of Science and Technology of Taiwan under research grant MOST-107-2115-M-009-016-MY3 and NCTS.

Appendix. Derivation of the elastic tension force on a triangulated surface

Consider a discrete closed surface composed of the N_T-number of triangles and the N_V-number of vertices correspondingly. The elastic tension is defined at the triangular center denoted by σ^i. Based on the same notations used in Section 2, and referring to the triangular area formula in Eq. (9), the discrete energy of elastic tension as an approximation of

$$E[\mathbf{X}] := \int_\Gamma \sigma \, \mathrm{d}A = \iint \sigma(\alpha,\beta)\|\mathbf{X}_\alpha \times \mathbf{X}_\beta\|_2 \, \mathrm{d}\alpha \, \mathrm{d}\beta$$

is given by

$$E_h[\mathbf{X}_1,\ldots,\mathbf{X}_{N_V}] := \sum_{i=1}^{N_T} \sigma^i \mathrm{d}A^i = \frac{1}{2}\sum_{i=1}^{N_T} \sigma^i \, \|(\mathbf{X}_2^i - \mathbf{X}_1^i)\times(\mathbf{X}_3^i - \mathbf{X}_1^i)\|_2.$$

The discrete energy on the triangulated surface perturbed at $\mathbf{X}_k$ by $\varepsilon\mathbf{Y}_k$ for all k can be written by

$$\begin{aligned}
&E_h[\mathbf{X}_1+\varepsilon\mathbf{Y}_1,\ldots,\mathbf{X}_{N_V}+\varepsilon\mathbf{Y}_{N_V}] \\
=&\frac{1}{2}\sum_{i=1}^{N_T}\sigma^i \left\| [(\mathbf{X}_2^i+\varepsilon\mathbf{Y}_2^i)-(\mathbf{X}_1^i+\varepsilon\mathbf{Y}_1^i)]\times[(\mathbf{X}_3^i+\varepsilon\mathbf{Y}_3^i)-(\mathbf{X}_1^i+\varepsilon\mathbf{Y}_1^i)] \right\|_2 .
\end{aligned}$$

Similar to the continuous case, by taking the derivative of the discrete perturbed energy with respect to ε, using the relation $\frac{d\|\mathbf{F}(\varepsilon)\|_2}{d\varepsilon} = \frac{\mathbf{F}(\varepsilon)}{\|\mathbf{F}(\varepsilon)\|_2}\cdot\frac{d\mathbf{F}(\varepsilon)}{d\varepsilon}$ and setting $\varepsilon = 0$, we have

$$\begin{aligned}
&\frac{\mathrm{d}}{\mathrm{d}\varepsilon}E_h[\mathbf{X}_1+\varepsilon\mathbf{Y}_1,\ldots,\mathbf{X}_{N_V}+\varepsilon\mathbf{Y}_{N_V}]\Big|_{\varepsilon=0} \\
=&\frac{1}{2}\sum_{i=1}^{N_T}\sigma^i \frac{[(\mathbf{X}_2^i+\varepsilon\mathbf{Y}_2^i)-(\mathbf{X}_1^i+\varepsilon\mathbf{Y}_1^i)]\times[(\mathbf{X}_3^i+\varepsilon\mathbf{Y}_3^i)-(\mathbf{X}_1^i+\varepsilon\mathbf{Y}_1^i)]}{\left\|[(\mathbf{X}_2^i+\varepsilon\mathbf{Y}_2^i)-(\mathbf{X}_1^i+\varepsilon\mathbf{Y}_1^i)]\times[(\mathbf{X}_3^i+\varepsilon\mathbf{Y}_3^i)-(\mathbf{X}_1^i+\varepsilon\mathbf{Y}_1^i)]\right\|_2} \\
&\cdot\left\{(\mathbf{Y}_2^i-\mathbf{Y}_1^i)\times[(\mathbf{X}_3^i+\varepsilon\mathbf{Y}_3^i)-(\mathbf{X}_1^i+\varepsilon\mathbf{Y}_1^i)]+[(\mathbf{X}_2^i+\varepsilon\mathbf{Y}_2^i)-(\mathbf{X}_1^i+\varepsilon\mathbf{Y}_1^i)]\times(\mathbf{Y}_3^i-\mathbf{Y}_1^i)\right\}|_{\varepsilon=0} \\
=&\frac{1}{2}\sum_{i=1}^{N_T}\sigma^i \frac{(\mathbf{X}_2^i-\mathbf{X}_1^i)\times(\mathbf{X}_3^i-\mathbf{X}_1^i)}{\left\|(\mathbf{X}_2^i-\mathbf{X}_1^i)\times(\mathbf{X}_3^i-\mathbf{X}_1^i)\right\|_2}\cdot\left[(\mathbf{Y}_2^i-\mathbf{Y}_1^i)\times(\mathbf{X}_3^i-\mathbf{X}_1^i)+(\mathbf{X}_2^i-\mathbf{X}_1^i)\times(\mathbf{Y}_3^i-\mathbf{Y}_1^i)\right] \\
=&\frac{1}{2}\sum_{i=1}^{N_T}\sigma^i\mathbf{n}_i\cdot\left[(\mathbf{Y}_2^i-\mathbf{Y}_1^i)\times(\mathbf{X}_3^i-\mathbf{X}_1^i)+(\mathbf{X}_2^i-\mathbf{X}_1^i)\times(\mathbf{Y}_3^i-\mathbf{Y}_1^i)\right] \\
=&\frac{1}{2}\sum_{i=1}^{N_T}\sigma^i\mathbf{n}_i\cdot\left[(\mathbf{X}_3^i-\mathbf{X}_2^i)\times\mathbf{Y}_1^i+(\mathbf{X}_1^i-\mathbf{X}_3^i)\times\mathbf{Y}_2^i+(\mathbf{X}_2^i-\mathbf{X}_1^i)\times\mathbf{Y}_3^i\right] \\
=&-\frac{1}{2}\sum_{i=1}^{N_T}\left[\sigma^i(\mathbf{X}_3^i-\mathbf{X}_2^i)\times\mathbf{n}_i\right]\cdot\mathbf{Y}_1^i+\left[\sigma^i(\mathbf{X}_1^i-\mathbf{X}_3^i)\times\mathbf{n}_i\right]\cdot\mathbf{Y}_2^i+\left[\sigma^i(\mathbf{X}_2^i-\mathbf{X}_1^i)\times\mathbf{n}_i\right]\cdot\mathbf{Y}_3^i \\
&\text{(by scalar triple product)} \\
=&-\sum_{k=1}^{N_V}\left(\sum_{i\in T(\mathbf{X}_k)}\frac{\sigma^i}{2}\left(\mathbf{X}_3^i-\mathbf{X}_2^i\right)\times\mathbf{n}_i\right)\cdot\mathbf{Y}_k \quad \text{(by the rearrangement of terms at each vertex)} \\
=&-\sum_{k=1}^{N_V}[\mathbf{F}_\sigma(\mathbf{X}_k)\,\mathrm{d}A(\mathbf{X}_k)]\cdot\mathbf{Y}_k \quad \text{(by the principle of virtual work).}
\end{aligned}$$

Consequently, the actual force of variable elastic tension at the k-th vertex $\mathbf{X}_k$ is computed by

$$\mathbf{F}_\sigma(\mathbf{X}_k)\,\mathrm{d}A(\mathbf{X}_k) = \sum_{i\in T(\mathbf{X}_k)}\frac{\sigma^i}{2}\left(\mathbf{X}_3^i-\mathbf{X}_2^i\right)\times\mathbf{n}_i. \tag{31}$$

This formula is similar to the one used to compute the mean curvature vector for constant tension σ in [15,28], refer also [8] and [32, Ch. 7.2.2].

References

[1] D. Abreu, M. Levant, V. Steinberg, U. Seifert, Fluid vesicles in flow, Adv. Colloid Interface Sci. 208 (2014) 129–141.
[2] S. Aland, S. Egerer, J. Lowengrub, A. Voigt, Diffuse interface models of locally inextensible vesicles in a viscous fluid, J. Comput. Phys. 277 (2014) 32–47.
[3] D. Barthès-Biesel, J.M. Rallison, The time-dependent deformation of a capsule freely suspended in a linear shear flow, J. Fluid Mech. 113 (1981) 251–267.
[4] T. Biben, K. Kassner, C. Misbah, Phase-field approach to three-dimensional vesicle dynamics, Phys. Rev. E 72 (2005) 041921.
[5] G. Boedec, M. Leonetti, M. Jaeger, 3D vesicle dynamics simulations with a linearly triangulated surface, J. Comput. Phys. 230 (2011) 1020–1034.
[6] K.-Y. Chen, K.-A. Feng, Y. Kim, M.-C. Lai, A note on pressure accuracy in immersed boundary method for Stokes flow, J. Comput. Phys. 230 (2011) 4377–4383.
[7] M.P. do Carmo, Differential Geometry of Curves and Surfaces, Pearson, 2009.
[8] T.G. Fai, B.E. Griffith, Y. Mori, C.S. Peskin, Immersed boundary method for variable viscosity and variable density problems using fast constant-coefficient linear solvers I: numerical method and results, SIAM J. Sci. Comput. 35 (2013) B1132–B1161.
[9] A. Farutin, T. Biben, C. Misbah, 3D numerical simulations of vesicle and inextensible capsule dynamics, J. Comput. Phys. 275 (2014) 539–568.
[10] A. Goza, S. Liska, B. Morley, T. Colonius, Accurate computation of surface stresses and forces with immersed boundary methods, J. Comput. Phys. 321 (2016) 860–873.
[11] W. Helfrich, Elastic properties of lipid bilayers: theory and possible experiments, Z. Naturforsch. C 28 (1973) 693–703.
[12] W.-F. Hu, Y. Kim, M.-C. Lai, An immersed boundary method for simulating the dynamics of three-dimensional axisymmetric vesicles in Navier-Stokes flows, J. Comput. Phys. 257 (2014) 670–686.
[13] S.R. Keller, R. Skalak, Motion of a tank-treading ellipsoidal particle in a shear flow, J. Fluid Mech. 120 (1982) 27–47.
[14] Y. Kim, M.-C. Lai, Simulating the dynamics of inextensible vesicles by the penalty immersed boundary method, J. Comput. Phys. 229 (2010) 4840–4853.
[15] Y. Kim, M.-C. Lai, C.S. Peskin, Y. Seol, Numerical simulations of three-dimensional foam by the immersed boundary method, J. Comput. Phys. 269 (2014) 1–21.
[16] E.M. Kolahdouz, D. Salac, Electrohydrodynamics of three-dimensional vesicles: a numerical approach, SIAM J. Sci. Comput. 37 (3) (2015) B473–B494.
[17] M. Kraus, W. Wintz, U. Seifert, R. Lipowsky, Fluid vesicles in shear flow, Phys. Rev. Lett. 77 (1996) 3685–3688.
[18] M.-C. Lai, W.-F. Hu, W.-W. Lin, A fractional step immersed boundary method for Stokes flow with an inextensible interface enclosing a solid particle, SIAM J. Sci. Comput. 34 (2012) B692–B710.
[19] M.-C. Lai, Y. Seol, A short note on Navier-Stokes flows with an incompressible interface and its approximations, Appl. Math. Lett. 65 (2017) 1–6.
[20] M.-C. Lai, K.C. Ong, Unconditionally energy stable schemes for the inextensible interface problem with bending, SIAM J. Sci. Comput. 41 (2019) B649–B668.
[21] C. de Loubens, J. Deschamps, F. Edwards-Levy, M. Leonetti, Tank-treading of microcapsules in shear flow, J. Fluid Mech. 789 (2016) 750–767.
[22] H. Noguchi, G. Gompper, Shape transitions of fluid vesicles and red blood cells in capillary flows, Proc. Natl. Acad. Sci. USA 102 (2005) 14159–14164.
[23] K.C. Ong, M.-C. Lai, An immersed boundary projection method for simulating the inextensible vesicle dynamics, J. Comput. Phys. 408 (2020) 109277.
[24] C.S. Peskin, Numerical analysis of blood flow in the heart, J. Comput. Phys. 25 (1977) 220–252.
[25] C.S. Peskin, The immersed boundary method, Acta Numer. 11 (2002) 479–517.
[26] D. Salac, M. Miksis, A level set projection model of lipid vesicles in general flows, J. Comput. Phys. 230 (2011) 8192–8215.
[27] D. Salac, M.J. Miksis, Reynolds number effects on lipid vesicles, J. Fluid Mech. 711 (2012) 122–146.
[28] Y. Seol, W.-F. Hu, Y. Kim, M.-C. Lai, An immersed boundary method for simulating vesicle dynamics in three dimensions, J. Comput. Phys. 322 (2016) 125–141.
[29] R. Skalak, A. Tozeren, R.P. Zarda, S. Chien, Strain energy function of red blood cell membranes, Biophys. J. 13 (1973) 245–264.
[30] H.A. Stone, A simple derivation of the time-dependent convective-diffusion equation for surfactant transport along a deforming interface, Phys. Fluids A 2 (1) (1990) 111–112.
[31] K. Taira, T. Colonius, The immersed boundary method: a projection approach, J. Comput. Phys. 225 (2) (2007) 2118–2137.
[32] G. Tryggvason, R. Scardovelli, S. Zaleski, Direct Numerical Simulations of Gas-Liquid Multiphase Flows, Cambridge University Press, 2011.
[33] S.K. Veerapaneni, A. Rahimian, G. Biros, D. Zorin, A fast algorithm for simulating vesicle flows in three dimensions, J. Comput. Phys. 230 (2011) 5610–5634.
[34] C.-H. Wu, T.G. Fai, P.J. Atzberger, C.S. Peskin, Simulation of osmotic swelling by the stochastic immersed boundary method, SIAM J. Sci. Comput. 37 (4) (2015) B660–B688.
[35] X. Yang, X. Zhang, Z. Li, G.-W. He, A smoothing technique for discrete delta functions with application to immersed boundary method in moving boundary simulations, J. Comput. Phys. 228 (2009) 7821–7836.
[36] A. Yazdani, P. Bagchi, Three-dimensional numerical simulation of vesicle dynamics using a front-tracking method, Phys. Rev. E 85 (2012) 056308.
[37] N.J. Zabusky, E. Segre, J. Deschamps, V. Kantsler, V. Steinberg, Dynamics of vesicles in shear and rotational flows: modal dynamics and phase diagram, Phys. Fluids 23 (2011) 041905.
[38] H. Zhao, E.S.G. Shaqfeh, The dynamics of a vesicle in simple shear flow, J. Fluid Mech. 674 (2011) 578–604.
[39] H. Zhou, C. Pozrikidis, Deformation of liquid capsules with incompressible interfaces in simple shear flow, J. Fluid Mech. 283 (1995) 175–200.